Pore and solid characterizations of interfacial transition zone (ITZ) of mortar using micro-computed tomography images

Sang-Yeop Chung[1], Ji-Su Kim[2], Paul H. Kamm[3], Dietmar Stephan[4], Tong-Seok Han[5], and Mohamed Abd Elrahman[6]

[1]Dept. of Civil and Environmental Engineering, Sejong Univ., Seoul 05006, Republic of Korea

[2]Dept. of Civil and Environmental Engineering, Yonsei Univ., Seoul 03722, Republic of Korea

[3]Institute of Applied Materials, Helmholtz Centre Berlin, Berlin 14109, Germany

[4]Dept. of Civil Engineering, Technische Universität Berlin, Berlin 13355, Germany

[5]Dept. of Civil and Environmental Engineering, Yonsei Univ., Seoul 03722, Republic of Korea.

Email: tshan@yonse.ac.kr

[6]Structural Engineering Department, Mansoura University, Mansoura City 35516, Egypt

ABSTRACT

The interfacial transition zone (ITZ) in concrete is known as the weakest link of the material, and significantly affects the properties of concrete. This study aims to investigate the actual microstructure of the ITZ using micro-computed tomography (micro-CT) in 3D. For this purpose, high-resolution synchrotron micro-CT images of materials are used to visualize and examine the 3D ITZ of cement-based specimens. A set of mortar specimens with different water–cement (w/c) ratios as well as different aggregate types and sizes were prepared and compared to investigate the effect of each condition on the characteristics of the ITZ. The microstructural characteristics of the pores and the solid structures of the ITZ are characterized based on the information of grayscale images. The obtained results show the effective investigation on the pore and solid characteristics of the ITZ microstructure by using 3D nondestructive micro-CT; this approach is useful for further detailed investigation of the ITZ.

Keywords: mortar; interfacial transition zone (ITZ); micro-CT; porosity; microstructure.

INTRODUCTION

Concrete is the most widely used construction material. Because concrete has a heterogeneous characteristic, its components strongly affect the material properties. The components of concrete can be classified into three general categories: matrix (bulk cement paste), aggregates, and interfacial transition zone (ITZ) (Mehta and Monteiro 2015; Neville 2012). Among them, the ITZ is a region in the vicinity of aggregates and has different characteristics from the bulk cement paste and the aggregates. It is generally known that the ITZ exists in the form of a thin shell with a width between 20 and 50 μm around the aggregates, particularly around large aggregate particles (Scrivener et al. 2004b; Leemann et al. 2010; Scrivener et al. 1988). The ITZ is often treated as the weakest link of concrete because of its high porosity compared with that of the bulk cement paste and the aggregates (Ollivier et al. 1995; Bernard and Kamali-Bernard 2015); therefore, the characteristics of the ITZ significantly influence the mechanical properties of concrete.

Several studies have been performed to investigate the ITZ microstructure using various methods such as scanning electron microscopy (SEM), transmission electron microscopy (TEM) (Diamond and Huang 2001; Scrivener et al. 2004a; He et al. 2019; Gao et al. 2018; Richardson et al. 1993), X-ray diffraction (XRD) (Horne et al. 2007; Vargas et al. 2017), and nanoindentation (Xiao et al. 2013). Similar to other components in concrete, the properties of the ITZ are strongly influenced by the pore structure of this zone. The pore characteristics of the ITZ have been studied using various approaches, such as SEM (Bentur and Alexander 2000; Ke et al. 2010) and digital image processing (DIP) (Garboczi and Bentz 1991; Lo et al. 2008). Previously used methods have limitations because the specimen is easily damaged during the preparation or measurement process, and only two-dimensional (2D) information can be achieved.

To overcome the disadvantages of the employed methods, X-ray micro-computed tomography (micro-CT) can be used for investigating the microstructure of the ITZ. Micro-CT is a nondestructive approach used to measure the inner structure of a target material and has been utilized to examine various cement-based composites (Chotard et al. 2003; Chung et al. 2019; du Plessis and Boshoff 2019; Huang et al. 2013). Micro-CT has advantages over other characterization methods.

By using this approach, both cross-sectional (2D) and volumetric (3D) information can be achieved without damaging the material. In particular, the internal 3D structure of a target material can be obtained using micro-CT, and further investigation such as component distribution and numerical analysis can be conducted using micro-CT data (Chung and Han 2013; Bossa et al. 2015; Kim et al. 2019a). The obtained 3D data is generally expressed as 8-bit or 16-bit grayscale images, and the information of a specific component (or phase) can be segmented using image processing techniques. For example, the pore structure, which is a dominant factor in determining the properties of concrete, has been investigated using micro-CT images. The pore characteristics of various cement-based materials, such as cement paste (Burlion et al. 2006), organic foamed concrete (Natesaiyer et al. 2015; Nambiar and Ramamurthy 2007), lightweight aggregate concrete (Chung et al. 2017; Lu et al. 2017), and porous concrete (Gallucci et al. 2007; Lu et al. 2006), have been evaluated using micro-CT. However, very few studies (Cui et al. 2017; Kim et al. 2019b) have been conducted on 3D ITZ analysis using micro-CT because high-resolution images with pixel sizes in micro units are required for ITZ investigation, while other image-based methods can present only 2D information in general (Gao et al. 2005; Lu et al. 2020). The use of 3D data based on micro-CT images can overcome the limitations of the 2D sectional analysis approach (Chen et al. 2016) and provide detailed information from real-shaped aggregate particles (Zhu et al. 2018).

This study aimed at visualizing the ITZ of cement-based materials in 3D, and quantitatively characterizing its microstructure using only micro-CT. For this purpose, high-resolution micro-CT was only used without the use of other investigation approaches. The resolution of micro-CT images depends significantly on the size of the target specimen. Moreover, very high-resolution images with pixel size in the order of less than a few micrometers are needed for effective description of the ITZ because its width is known to be less than 50 μm in general. To achieve micro-CT images with pixel sizes less than 1 μm, a set of mortar specimens was produced using a thin glass tube. The high-resolution micro-CT images were obtained from the high-energy synchrotron micro-CT facility at the beamline 6C (BMI) of Pohang Accelerator Laboratory (PAL) in the Republic of Korea. Several studies have reported that the characteristics of the aggregates,

such as size (Nadeau 2003; Elsharief et al. 2003; Chen et al. 2011), shape (Scrivener et al. 2004a; Chen et al. 2016), and volume fraction (Zheng et al. 2011), can affect the ITZ structures. Thus, specimens with different aggregate types and water–cement ratios (w/c) were produced to evaluate their effects on the ITZ structures. The ITZ characteristics of aggregates with different sizes are also examined, and the pore and solid structures of their ITZs are compared in 3D. The following section presents a detailed description of the sample preparation, and the micro-CT imaging procedure is introduced in Section 3. Then, the ITZs of all cases in this study are characterized and compared in terms of aggregate types, w/c ratio, and aggregate particle size. Finally, the results of this study are summarized in the Discussions and the Conclusions.

SPECIMEN PREPARATION

The main objective of this study is to visualize and characterize the microstructure of the ITZ in 3D. For this purpose, micro-CT is adopted to obtain the microstructural information of the ITZ, and the high-resolution CT images are needed for its characterization. Because the image resolution of micro-CT is correlated strongly with the sample size, an appropriate specimen size is important for more effective measurement.

To produce a specimen with a proper size which allows for an adequate spatial resolution, a set of mortar samples 70 mm in length and 0.9 mm in diameter were produced using a glass tube; this sample size represents the optimal size that can effectively be measured at the micro-CT facility at PAL. The specimens were molded, cured, and measured in a glass tube. In the preparation process, a small mixer was used to mix the constituents together without agglomeration or clumps. Water was first added to the mixer, and then the cement and aggregates were added. Aggregates were used in dry conditions, and water equivalent to the amount absorbed by the aggregate was added to the mixing water. In the preparation process, a hand mixer with different levels of rotational speed up to 1200 rpm was used to mix the components. A total of 300 ml of mortar was mixed in a half-liter rubber bucket. The mixing period was 3 min; the mixing was performed for 1 min, after which 1 min was expended to remove the mortar stuck to the sides of the mixer, and finally, the mixture was mixed for 1 min. Owing to the relatively small diameter of the used tubes (0.9

mm), the used mortar should have high workability and fluidity. Therefore, a superplasticizer was used for the mixture with w/c 0.4 to achieve the required workability. After mixing, the glass tubes with lengths and diameters of 70 and 0.9 mm, respectively, were filled with mortar. The tubes were filled by injection using a syringe with an opening diameter of approximately 0.73 mm without a needle. To fill the tube, water-reducing admixture was added to the mixes at a low w/c ratio (0.4) to produce flowable mortar with an appropriate consistency and further prevent the blocking of the tubes. The tubes were compacted by jolting them gently to remove air bubbles. Thereafter, the specimens were sealed in closed plastic bags to prevent evaporation of the water. The curing process was conducted in a controlled curing chamber at a temperature of 21±1 °C and relative humidity of 99% before the testing.

Refs. (Neville 2012; Scrivener et al. 2004b; Kong et al. 2014) reported that the characteristics of ITZ are affected by the aggregate type and size. In addition, the ITZ tends to have higher porosity than cement paste or binder (Mehta and Monteiro 2015; Mindess et al. 2002), and the w/c ratio, which is a dominant factor in determining the pore structure of cement-based materials, can affect the microstructure of the ITZ. Therefore, three conditions were considered to investigate the effect of each factor on the ITZ characteristics: aggregate type, w/c ratio, and aggregate size. Considering the aggregate type, quartz sand and limestone were used as fine aggregates, and particles with sizes between 0.1 and 0.3 mm were used for each aggregate type considering the size of the glass tube. The quartz sand is rounded with a smooth surface, while the limestone sand is polygonal (crushed) with a rough surface, which can affect the microstructural characteristics of ITZ (Mehta and Monteiro 2015; Lyu et al. 2019). To examine the effect of the w/c ratio on the ITZ, w/c ratios of 0.4 and 0.6 were selected. CEM I 52.5 R (HeidelbergCement, Germany) was used as the binder material, and polycarboxylic-ether-based superplasticizer (SP) with a density of 1.04 g/cm^3 was used for the specimens with a 0.4 w/c ratio to reach proper workability. In the case of mixes with a w/c value of 0.4, the water in the superplasticizer was included in the mixing water.

The chemical compositions of the used cement, and aggregates are given in Table 1, and the physical properties and particle-size distributions of the used cement and aggregates are presented

in Table 2 and Fig. 2, respectively. The detailed mix composition is presented in Table 3. Here, a set of mortar specimens were produced and investigated instead of concrete considering the optimal sample size. The specimens with quartz sand were denoted as 'Quartz' with the w/c ratio level; other specimens containing limestone were denoted as 'Limestone'.

MICRO-CT IMAGE AND ITZ CHARACTERIZATION

Micro-CT images are used to nondestructively visualize the inner structure of a target material; they were thus used for examining the ITZ structures of the specimens. With the obtained 3D microstructure of the ITZ, its pore and solid structure characteristics, such as porosity gradient, were quantitatively investigated.

Micro-CT imaging procedure

Several approaches such as SEM (Ke et al. 2010) and DIP (Lo et al. 2008) have been adopted to identify the ITZ of cement-based materials. However, such methods are limited for quantifying and describing the volumetric characteristics of the ITZ. To visualize and investigate the ITZ structure in 3D, micro-CT is utilized in this study. X-ray images were obtained using a synchrotron at the Pohang Accelerator Laboratory (PAL) of South Korea. The energy level and distance between the sample and detector were set at 25 keV and 30 mm, respectively. The double crystal monochromator (DCC) equipped with Si (111) reflection was used to produce a monochromatic X-ray beam. For each specimen, a total of 360 projection images were obtained with an incremental rotation degree of 0.5° per projection with the total rotation degree of 180°. Further, the exposure time was 2000 ms per projection.

Fig. 3 shows the image processing procedure used to classify aggregates from an original micro-CT image for the ITZ investigation. For effective investigation of the specimens, a region of interest (ROI), which includes a sufficient number of aggregate particles, is selected from each case. The image in this figure is composed of 800×800 pixels at a size of 0.65 μm. Fig. 3(a) shows an example of the 8-bit original micro-CT image. Each pixel in this image is represented by an 8-bit integer value between 0 and 255 in grayscale. The gray level becomes darker (black) as the value approaches zero. Because the target object of this study is the ITZ in the vicinity of the

aggregates, segmentation of the aggregates from an original image must first be conducted. The initially binarized image in Fig. 3(b) is obtained by thresholding the 8-bit image. To enhance the image contrast and to select a proper threshold value, image contrasting is performed to adjust the image histogram, and the value is determined using the modified Otsu method (Otsu 1979) as well as manual selection, respectively. In the initial binary image, the aggregates and other fragments are represented in white, whereas the binder is shown in grayscale. Here, most of the fragments are found near the aggregates owing to the heterogeneous structure of the binder material and their pixel values reflecting the relative density. For a clearer segmentation of aggregates, morphology (Gonzalez et al. 2004) and edge detection (Canny 1986) algorithms are used in which only the target regions of the aggregates are segmented successfully, as shown in Fig. 3(c). The segmented image in Fig. 3(d) is then obtained by overlying the original micro-CT image (Fig. 3(a)) with the modified binary image (Fig. 3(c)). In this image, only the relatively large aggregates are described in white, whereas the binder (or cement stone) is represented as it is in the 8-bit image.

The ITZ investigation is performed by stacking a series of segmented images in 3D. After separating the aggregates from the binder, pores inside the sample are identified. Because the aim of this study was to investigate the pore gradient near the ITZ, pore segmentation was conducted concentrically in the region of the ITZ, which will be further discussed in the following sections. To evaluate the porosity characteristics of ITZ, a threshold value for pores was selected using the histogram information of ITZ and the modified Otsu method (Otsu 1979). For instance, the grayscale histogram of the Quartz04 specimen presented in Fig. 4 shows the grayscale distributions of the entire phases and pore/aggregates as solid and dashed lines, respectively. The complete process is performed using the image toolbox in MATLAB (R2018a) (MATLAB 2018).

ITZ structure characterization

The width of the ITZ is known to be 20 to 50 μm in the vicinity of an aggregate (Scrivener et al. 2004b; Leemann et al. 2010). The microstructure of the ITZ differs from that of the bulk paste because the particles that occur near aggregates are loosely packed, and the bulk paste exhibits lower porosity (Mehta and Monteiro 2015; Neville 2012). In addition, the porosity of the ITZ

shows variation with distance from the aggregate surface with the porosity gradient occurring perpendicular to the aggregate surface (Neville 2012; Kim et al. 2019b). Although the gradient characteristics of pores in the ITZ have been investigated, such research has considered only cross-sectional information along a specific direction (Scrivener et al. 2004a; Gao et al. 2013) or limited volumetric information (Lukovic and Ye 2016; Zhang et al. 2019).

In this study, the volumetric characteristics of ITZ for both solid and pore structures are identified using the micro-CT images.

Fig. 5 shows a schematic diagram of the ITZ investigation. In Figs. 5(a) and (d), the part in closest proximity to the aggregates is darker than the binder part with distance from the aggregates, e.g., the marked region in Fig. 5(d). The ITZ information is collected from the image showing segmented aggregates in Fig. 5(b). Here, all micro-CT images have the same resolution of 0.65 μm pixel size. Previous studies by Refs. (Kim et al. 2019b; Gao et al. 2013) show that the ITZ microstructure has gradient characteristics. In this study, these spatial effects were analyzed by dividing the ITZ into layers based on the number of pixels (or voxels), as shown in Figs. 5(c) and (e). Because the voxel size of the image used is 0.65 μm, the general ITZ of concrete can be described with 30 (20 μm) to 77 (50 μm) voxels, which is sufficient for investigating the gradient effect. Here, the width of the ITZ is assumed to be about 70 μm for effective investigation of the gradient effect, and the entire ITZ is divided into 18 layers. The width of each layer is composed of 6 voxels (3.9 μm), and the gradation of the pores and solid area is examined layer-by-layer. Problems pertaining to interactions between aggregates have been reported in ITZ investigations (Lu et al. 2020; Xu et al. 2013; Lin et al. 2019), and the similar trend was also observed in this study. Here, the overlapped ITZ regions within 70 μm were not considered in the calculation, and all characteristics were computed using information from non-overlapping regions. Based on the procedure described in the schematic in Fig. 5, the ITZ investigation was performed in 3D so that the volumetric characteristics could be identified. For detailed investigation of the ITZ, the grey values in each layer are collected, and their mean values are computed. With the 3D micro-CT images and collected data, the effects of the w/c ratio, aggregate type, and aggregate size on the

ITZ characteristics are investigated.

CHARACTERIZATION OF ITZ

The ITZ in various mortar specimens is investigated using the volumetric data obtained from high-resolution micro-CT images. The ITZ characteristics were visualized using 3D microstructure images, and the ITZs of the specimens with different w/c ratios, aggregates types, and aggregate sizes were compared. The influence of each condition on the ITZ structure was examined using the 3D microstructural information.

Effects of w/c ratio and aggregate type on ITZ

The ITZs of the specimens were investigated in 3D on the basis of the ROI ($520\times520\times520$ μm^3) of each case in Fig. 6. In these images, aggregate particles (quartz sand or limestone) are shown in colors that differ from those of the binder, and the aggregates have relatively homogeneous grayscale whereas that of the binder is heterogeneous. In the heterogeneous binder, several bright particles can be found, which are assumed to be unhydrated materials remaining in the specimen, caused by insufficient reaction with water. By following the procedure introduced in Section 3.2, the characteristics of the ITZ in each specimen were investigated. Fig. 7 shows the averaged porosity distribution near the aggregate particles in each specimen. Based on the image resolution, only pores with larger diameters than the voxel size (0.65 μm) were considered in the porosity measurement. In each figure, the gray represents the aggregate particles. In all cases, a porosity gradient can be identified, where the regions in close proximity to the aggregates show higher porosity. Porosity decreases with increasing distance from the aggregates; the degree of porosity gradient is more evident in the Quartz specimens than in the Limestone specimens. In Fig. 7, the porosity of the binder in the Quartz specimens is lower than that of the Limestone specimens, which denotes a denser solid structure. Considering the difference in relative density of the binders, a porosity gradient is generally more distinct in the vicinity of quartz sand than that of limestone. The porosity gradient in the Quartz specimens, particularly the Quartz04 specimen, is clearly shown in the images. The change in the porosity in the Limestone specimens is less obvious, although the trend of a gradient is shown. The size of the porosity gradient in the ITZ

represents its microstructural characteristics. The Quartz04 specimen has a narrower ITZ than that with a larger w/c ratio (Quartz06) and with limestone at the same w/c (Limestone04), although its porosity gradient is larger than that of the other cases in this study. With the same aggregates, the ITZ width and the porosity of both the ITZ and the binder increased as the w/c increased. At the same w/c level, the Quartz specimens contain narrower but clearer ITZ than the Limestone specimens. Hence, the specimens with quartz sand tend to show an ITZ distinct from its binder, whereas the ITZ of the Limestone specimens shows a relatively small difference.

All the characteristics of the ITZ were quantitatively investigated according to the 3D images of the microstructures, as shown in Fig. 7. Information of the porosity and the mean voxel value of the ITZ is plotted in Fig. 8. In this study, the ITZ characteristics up to a distance of 70 μm were measured, which is sufficient for effective ITZ analysis considering the distance between the aggregates. Fig. 8 shows the averaged data of the ITZ characteristics in each specimen so that an overall trend according to the different aggregate types and w/c ratios can be identified. Here, the mean voxel grayscale vale is the average voxel value of each ITZ layer and can be used to describe the relative solid densities of the ITZs. Each characteristic profile is the average of the values obtained from the ITZ near all aggregates inside each specimen. In each step, approximately 6.7–9.8 million elements, depending on the aggregate types and sizes, were considered for the investigation of the ITZ characteristics. In fact, the value at x=0 in Fig. 8(a) should be zero, but the average value for the 1^{st} interval is assigned for a visualization purpose. The change in porosity with respect to the distance from the aggregates in Fig. 8(a) clearly shows a gradient for each specimen, which is consistent with the results in (Chen et al. 2007; Latham et al. 2019); this trend is clearer in the Quartz specimens. In all cases, the porosity decreases as the distance from the aggregate increases. Both Quartz04 and Quartz06 show a porosity larger than 0.5 in the vicinity of the aggregates; the porosity significantly decreases in the region away from the aggregates. This trend is less clear in the Limestone specimens, although the porosity decreases about 10 and 20% at 70 μm from the aggregates of the Limestone06 and Limestone04, respectively.

Fig. 8(b) presents the mean voxel value of the ITZ in each specimen. In the micro-CT images,

each voxel value is correlated with a particle density, where a larger voxel value denotes a relatively denser structure of the solid. In all specimens, the voxel values increase with the distance from the aggregates, which indicates that the microstructure of the ITZ near aggregates is sparser and becomes denser as the distance increases. In addition, for w/c ratios of 0.4 and 0.6, the Limestone specimen shows a higher mean voxel value in the coverage distance, which indicates that the solid structures of the Limestone specimens are denser than that of the Quartz specimens; this denotes that limestone aggregates tend to improve packing of cement grains so to have denser solid structures. As shown in Figs. 7 and 8, the general characteristics of the ITZ according to the w/c ratio and aggregate type can be identified using the micro-CT images. Under the same conditions, a material with quartz sand tends to have ITZ with a porosity gradient, and the microstructural difference between the ITZ and the binder becomes distinct when containing a lower w/c ratio. The general trend of average porosity in Fig. 8 is similar to the results obtained in previous studies (Chen et al. 2007; Larbi et al. 2016). In addition to the general trend of porosity, the effects of the type and size of each aggregate on the ITZ characteristics are evaluated in the following section.

Effects of aggregate size and shape on ITZ

The effect of aggregate size on the ITZ characteristics was also evaluated using the micro-CT-based approach, in which 8–16 aggregate particles with different sizes were selected from each specimen. In the ROI for each specimen, the maximum aggregate size was 140.2–182.6 μm. Fig. 9 illustrates the porosity data of the aggregates with different sizes with distance from them. The horizontal axes represent the relative size of the chosen aggregates, which is normalized to that of the largest aggregate in each specimen so that the maximum relative aggregate size is 1, and the distance of the considered ITZ layer from their surface. The vertical axis represents the associated porosity.

As shown in Fig. 9(a), a porosity gradient is clearly visible in the Quartz04 specimen. In this specimen, the porosity of the ITZ tends to increase in larger aggregates, and the gradient tendency is similar to that shown in Fig. 8(a). In contrast, the Quartz06 specimen shows little change

in porosity as the aggregate size changes, though the gradient trend with the distance is almost identical to the mean porosity shown in Fig. 8(a). The Limestone specimens show a similar porosity characteristic. In the specimen with 0.4 w/c ratio, the trend of the porosity gradient changes depending on the aggregate size, whereas the porosity gradient is generally consistent in the Limestone06 specimen. In both Limestone04 and 06 specimens, inconsistent porosity changes were found when the aggregate size is very small (< 0.3 relative size). The distribution of the mean voxel values shown in Fig. 10 represents a similar trend of the ITZ characteristics; the specimens with 0.4 w/c ratio show a change in gradient depending on the aggregate size, whereas the 0.6 specimens show less gradient in the overall aggregate size. In addition, the Quartz06 specimen shows a change in voxel value. In the case of porosity, the value decreases with increasing distance from aggregates, while the mean voxel value increases; this is because a high porosity is related to a relatively sparse or weak solid structure. The obtained results confirm that the ITZ characteristics depend on the w/c ratio as well as the aggregate type and size. Compared with the specimens containing limestone, the specimen with quartz sand aggregates show a clearer ITZ with a porosity gradient; this phenomenon is more pronounced in samples with a smaller w/c ratio and larger aggregate size.

In addition to the aggregate size, the effect of the aggregate shape on the ITZ pore characteristics was also investigated. Aggregate shape is considered to be an important factor that affects the ITZ properties (Mehta and Monteiro 2015; Neville 2012), and a better understanding of the particle shape could contribute to the ITZ characterization. From micro-CT images, a 3D morphology of the used aggregate particles can be visualized. To characterize the aggregate shape, Wadell's sphericity, a parameter that indicates the degree of equiaxed-particle shape, was used. Wadell's sphericity (S_w) is defined as the ratio of the surface area of a sphere having the same volume as the particle (S_s) and the actual surface area of a particle (S) (Bullard and Garboczi 2013):

$$S_w = \frac{S_s}{S} \tag{1}$$

Eq. (1) is a value between 0 and 1, and a value of 1 for S_w indicates a complete sphere. Using this

parameter, the anisotropic degree of aggregates can be examined.

Fig. 11 shows the porosity gradient of the aggregates with different sphericities. The horizontal axes represent the Wadell's sphericity of the considered aggregates. The measured aggregates in this study had sphericities between 0.5 and 0.85, and 8-16 aggregates with different sphericity values were considered from each specimen. In Fig. 11, a general trend of each aggregate type can be found. The aggregates in the Quartz specimens tend to be rounder than those in the Limestone specimens, particularly when the w/c ratio is 0.4. Within the considered range of the Wadell's sphericity, an evident porosity gradient is visible in the Quartz specimens, and the degree of the gradient is clearer when the sphericity is between 0.7 and 0.8; this denotes that the shape of Quartz aggregates has lesser impact on the ITZ characteristics than the particle size. For the Limestone specimens in Figs. 11(c) and (d), the porosity gradient tends to be clear when the sphericity is less than 0.6. Since a lower sphericity value indicates less roundness of a particle, the result in Fig. 11 shows the effect of the limestone shape; the anisotropy of the particles affects the degree of the porosity gradient, though its impact is less significant than that of the aggregate size.

CONCLUSIONS

The main objective of this study was to visualize and investigate the ITZ characteristics of mortar specimens in different conditions. For this purpose, a 3D microstructural characterization of ITZ using micro-CT only was presented. The ITZ structure of mortar specimens was visualized and investigated in 3D, whereas previous studies have focused on the ITZ investigation for a limited region in 2D. For comparison, a set of specimens with different w/c ratios of 0.4 and 0.6 and different aggregates of quartz sand and limestone were prepared, and the effect of aggregate size on the microstructure of the ITZ was examined. To achieve high-resolution micro-CT images that can effectively illustrate the ITZ, a high-energy synchrotron facility was used. The mortar samples were produced in a very thin glass tube so that a high-resolution image could be generated. A series of micro-CT measurements with a 0.65 μm voxel size were used, which was sufficient for describing an ITZ with a width of 20-50 μm.

The concluding remarks of this study can be summarized as follows:

- The use of high-resolution micro-CT images with a very small voxel size (< 1 μm) can effectively show the 3D microstructure of the ITZ without damaging the specimen. With the obtained micro-CT images, the spatial pore and solid characteristics of the ITZ can be effectively described using the proposed imaging approach.

- The porosity gradient and the mean voxel values related to the relative material density can be successfully described using micro-CT images. In particular, the difference between the ITZ of the specimens in different conditions, such as w/c ratio and aggregate type and size as well as shape, can be investigated qualitatively and quantitatively.

- Among the cases evaluated here, the specimen containing quartz sand showed a more distinct ITZ with a porosity gradient than the specimens containing limestone. This trend was clear in the specimen with a smaller w/c ratio in the vicinity of larger aggregate particles.

Future work should focus on a case study that uses concrete specimens with different aggregate types and curing conditions, and higher-resolution CT images can be used to more effectively explain additional detailed features of the ITZ microstructure. In addition to the results of this study, other investigation approaches, such as SEM and XRD, can be used as complementary methods for a more detailed evaluation of the microstructural characteristics.

DATA AVAILABILITY STATEMENT

Some or all data, models, or code that support the findings of this study are available from the corresponding author upon reasonable request.

ACKNOWLEDGMENTS

The project is supported by the German Federal Ministry of Education and Research (BMBF, Project Number: 41413XP5010B); the Korea Agency for Infrastructure Technology Advancement (KAIA) grant funded by the Ministry of Land, Infrastructure and Transport (Grant 21NANO-B156177-02); and the KOREA HYDRO & NUCLEAR POWER CO., LTD (No. 2019-TECH-01).

The micro-CT images were obtained from the synchrotron operated by the Pohang Accelerator Laboratory (PAL) in the Republic of Korea.

REFERENCES

Bentur, A. and Alexander, M. G. (2000). "A review of the work of the RILEM TC 159-ETC: Engineering of the interfacial transition zone in cementitious composites." *Materials and Structures*, 33, 82–87.

Bernard, F. and Kamali-Bernard, S. (2015). "Numerical study of ITZ contribution on mechanical behavior and diffusivity of mortars." *Computational Materials Science*, 102, 250–257.

Bossa, N., Chaurand, P., Vicente, J., Borschneck, D., Levard, C., Chariol, O. A., and Rose, J. (2015). "Micro- and nano-x-ray computed-tomography: A step forward in the characterization of the pore-network of a leached cement paste." *Cement and Concrete Research*, 67, 138–147.

Bullard, J. and Garboczi, E. (2013). "Defining shape measures for 3d star-shaped particles: Sphericity, roundness, and dimensions." *Powder technology*, 249, 241–252.

Burlion, N., Bernard, D., and Chen, D. (2006). "X-ray microtomography: application to microstructure analysis of a cementitious material during leaching process." *Cement and Concrete Reaserch*, 36, 346–357.

Canny, J. (1986). "A computational approach to edge detection." *IEEE Transactions on Pattern Analysis and Machine Intelligence*, 6, 679–698.

Chen, H., Sluys, L., Stroeven, P., and Sun, W. (2011). "Theoretical prediction on thickness distribution of cement paste among neighboring aggregates in concrete." *Computers and Concrete*, 8(2), 163–176.

Chen, H., Sun, W., Zhao, Q., Sluys, L., and Stroeven, P. (2007). "Effects of fiber curvature on the microstructure of the interfacial transition zone in fresh concrete." *Frontiers of Architecture and Civil Engineering in China*, 1(1), 99–106.

Chen, H., Zhu, Z., Liu, L., Sun, W., and Miao, C. (2016). "Aggregate shape effect on the overestimation of ITZ thickness: Quantitative analysis of platonic particles." *Powder technology*, 289, 1–17.

399 Chotard, T., Boncoeur-Martel, M., Smith, A., Dupuy, J., and Gault, C. (2003). "Application of
400 X-ray computed tomography to characterise the early hydration of calcium aluminate cement."
401 *Cement and Concrete Composites*, 25, 145–152.
402 Chung, S.-Y., Elrahman, M. A., Kim, J.-S., Han, T.-S., Stephan, D., and Sikora, P. (2019). "Com-
403 parison of lightweight aggregate and foamed concrete with the same density level using image-
404 based characterizations." *Construction and Building Materials*, 211, 988–999.
405 Chung, S.-Y., Elrahman, M. A., and Stephan, D. (2017). "Effect of different gradings of lightweight
406 aggregates on the properties of concrete." *Applied Sciences*, 7, 585:1–15.
407 Chung, S.-Y. and Han, T.-S. (2013). "Correlation between low-order probability distribution func-
408 tions and percolation of porous concrete." *Magazine of Concrete Research*, 65, 448–460.
409 Cui, D., Sun, W., Wan, K., and Banthia, N. (2017). "Porosity characterization in interfacial transi-
410 tion zone using dual CT scans." *Journal of Testing and Evaluation*, 45, 408–418.
411 Diamond, S. and Huang, J. (2001). "The ITZ in concrete – a different view based on image analysis
412 and SEM observations." *Cement and Concrete Composites*, 23, 179–188.
413 du Plessis, A. and Boshoff, W. (2019). "A review of X-ray computed tomography of concrete and
414 asphalt construction materials." *Construction and Building Materials*, 199, 637–651.
415 Elsharief, A., Cohen, M. D., and Olek, J. (2003). "Influence of aggregate size, water cement ratio
416 and age on the microstructure of the interfacial transition zone." *Cement and Concrete Research*,
417 33, 1837–1849.
418 Gallucci, E., Scrivener, K., Groso, A., Stampanoni, M., and Margaritondo, G. (2007). "3D exper-
419 imental investigation of the microstructure of cement pastes using synchrotron X-ray microto-
420 mography." *Cement and Concrete Research*, 37, 360–368.
421 Gao, J. M., Qian, C. X., Liu, H. F., Wang, B., and Li, L. (2005). "ITZ microstructure of concrete
422 containing GGBS." *Cement and Concrete Research*, 35, 1299–1304.
423 Gao, Y., Hu, C., Zhang, Y., Li, Z., and Pan, J. (2018). "Characterisation of the interfacial transition
424 zone in mortars by nanoindentation and scanning electron microscope." *Magazine of Concrete
425 Research*, 70, 965–972.

Gao, Y., Schutter, G., Ye, G., Huang, H., Tan, Z., and Wu, K. (2013). "Porosity characterization of ITZ in cementitious composites: concentric expansion and overflow criterion." *Construction and Building Materials*, 38, 1051–1057.

Garboczi, E. and Bentz, D. (1991). "Digital simulation of the aggregate–cement paste interfacial zone in concrete." *Journal of Materials Research*, 6, 196–201.

Gonzalez, R. C., Woods, R. E., and Eddins, S. L. (2004). *Digital Image Processing Using MATLAB*. Pearson Prentice Hall, New Jersey.

He, S., Li, Z., and Yang, E.-H. (2019). "Quantitative characterization of anisotropic properties of the interfacial transition zone (ITZ) between microfiber and cement paste." *Cement and Concrete Research*, 122, 136–146.

Horne, A. T., Richardson, I. G., and Brydson, R. M. D. (2007). "Quantitative analysis of the microstructure of interfaces in steel reinforced concrete." *Cement and Concrete Research*, 37, 1613–1623.

Huang, J., Krabbenhoft, K., and Lyamin, A. (2013). "Statistical homogenization of elastic properties of cement paste based on X-ray microtomography images." *International Journal of Solids and Structures*, 50, 699–709.

Ke, Y., Ortola, S., Beaucour, A. L., and Dumontet, H. (2010). "Identification of microstructural characteristics in lightweight aggregates concretes by micromechanical modelling including the interfacial transition zone (ITZ)." *Cement and Concrete Research*, 40, 1590–1600.

Kim, J.-S., Chung, S.-Y., Stephan, D., and Han, T.-S. (2019a). "Issues on characterization of cement paste microstructures from μ-CT and virtual experiment framework for evaluating mechanical properties." *Construction and Building Materials*, 202, 82–102.

Kim, S.-Y., Kim, J.-S., Kang, J. W., and Han, T.-S. (2019b). "Construction of virtual interfacial transition zone (ITZ) samples of hydrated cement paste using extended stochastic optimization." *Cement and Concrete Composites*, 102, 84–93.

Kong, L., Gao, L., and Du, Y. (2014). "No access effect of coarse aggregate on the interfacial transition zone of concrete based on grey correlation." *Magazine of Concrete Research*, 66,

339–347.

Larbi, B., Dridi, W., Dangla, P., and Le Bescop, P. (2016). “Link between microstructure and tritiated water diffusivity in mortars: Impact of aggregates.” *Cement and Concrete Research*, 82, 92–99.

Latham, J.-P., Xiang, J., Farsi, A., Joulin, C., and Karantzoulis, N. (2019). “A class of particulate problems suited to fdem requiring accurate simulation of shape effects in packed granular structures.” *Computational Particle Mechanics*, 1–12.

Leemann, A., Loser, R., and Muench, B. (2010). “Influence of cement type on ITZ porosity and chloride resistance of self-compacting concrete.” *Cement and Concrete Composites*, 32, 116–120.

Lin, J., Chen, H., Zhang, R., and Liu, L. (2019). “Characterization of the wall effect of concrete via random packing of polydispersed superball-shaped aggregates.” *Materials Characterization*, 154, 335–343.

Lo, T. Y., Cui, H. Z., Tang, W. C., and Leung, W. M. (2008). “The effect of aggregate absorption on pore area at interfacial zoneof lightweight concrete.” *Construction and Building Materials*, 22, 623–628.

Lu, H., Alymov, E., Shah, S., and Peterson, K. (2017). “Measurement of air void system in lightweight concrete by X-ray computed tomography.” *Construction and Building Materials*, 152, 467–483.

Lu, S., Landis, E., and Keane, D. (2006). “X-ray microtomographic studies of pore structure and permeability in Portland cement concrete.” *Materials and Structures*, 36, 11–20.

Lu, Y., Islam, M., Thomas, S., and Garboczi, E. (2020). “Three-dimensional mortar models using real-shaped sand particles and uniform thickness interfacial transition zones: Artifacts seen in 2d slices.” *Construction and Building Materials*, 236, 117590.

Lukovic, M. and Ye, G. (2016). “Effect of moisture exchange on interface formation in the repair system studied by X-ray absorption.” *Materials*, 9, 2.

Lyu, K., Garboczi, E., She, W., and Miao, C. (2019). “The effect of rough vs. smooth aggregate sur-

faces on the characteristics of the interfacial transition zone." *Cement and Concrete Composites*, 99, 49–61.

MATLAB (2018). *R2018b*. The MathWorks Inc., Natick, Massachusetts.

Mehta, P. K. and Monteiro, P. J. M. (2015). *Concrete: microstructure, properties and materials, 4th Ed.* McGraw-Hill, New York.

Mindess, S., Young, J. F., and Darwin, D. (2002). *Concrete, 2nd Ed.* Prentice Hall, New York.

Nadeau, J. C. (2003). "A multiscale model for effective moduli of concrete incorporating ITZ water–cement ratio gradients, aggregate size distributions, and entrapped voids." *Cement and Concrete Research*, 33, 103–113.

Nambiar, E. K. and Ramamurthy, K. (2007). "Air–void characterisation of foam concrete." *Cement and Concrete Research*, 37, 221–230.

Natesaiyer, K., Chan, C., Sinha-Ray, S., Song, D., Lin, C. L., Miller, J. D., Garboczi, E. J., and Forster, A. M. (2015). "X–ray CT imaging and finite element computations of the elastic properties of a rigid organic foam compared to experimental measurements: insights into foam variability." *Journal of Materials Science*, 50, 4012–4024.

Neville, A. M. (2012). *Properties of concrete, 5th Ed.* Wiley, Chichester.

Ollivier, J., Maso, J., and Bourdette, B. (1995). "Interfacial transition zone in concrete." *Advanced Cement Based Materials*, 2, 30–38.

Otsu, N. (1979). "A threshold selection method from gray-level histograms." *Man and Cybernetics*, 9, 62–66.

Richardson, I. G., Hall, C., and Groves, G. W. (1993). "TEM study of the composition of the interstitial phase in an oil-well cement clinker." *Advances in Cement Research*, 5, 15–21.

Scrivener, K. L., Bentur, A., and Pratt, P. L. (1988). "Quantitative characterisation of the transitionzone in high strength concrete." *Advanced Cement Research*, 1, 230–237.

Scrivener, K. L., Grumbie, A., and Laugesen, P. (2004a). "Backscattered electron imaging of cementitious microstructures: understanding and quantification." *Cement and Concrete Composites*, 26, 935–945.

Scrivener, K. L., Grumbie, A., and Laugesen, P. (2004b). "The interfacial transition zone (ITZ) between cement paste and aggregate in concrete." *Interface Science*, 12, 411–421.

Vargas, P., Restrepo-Baena, O., and Tobon, J. I. (2017). "Microstructural analysis of interfacial transition zone (ITZ) and its impact on the compressive strength of lightweight concretes." *Construction and Building Materials*, 137, 381–389.

Xiao, J., Li, W., Sun, Z., Lange, D. A., and Shah, S. P. (2013). "Properties of interfacial transition zones in recycled aggregate concrete tested by nanoindentation." *Cement and Concrete Composites*, 37, 276–292.

Xu, W., Lv, Z., and Chen, H. (2013). "Effects of particle size distribution, shape and volume fraction of aggregates on the wall effect of concrete via random sequential packing of polydispersed ellipsoidal particles." *Physica A: Statistical Mechanics and its Applications*, 392(3), 416–426.

Zhang, H., Gan, Y., Xu, Y., Zhang, S., Schlangen, E., and Savija, B. (2019). "Experimentally informed fracture modelling of interfacial transition zone at micro-scale." *Cement and Concrete Composites*, 104, 103383.

Zheng, J. J., Guo, Z. Q., Pan, X. D., Stroeven, P., and Sluys, L. H. (2011). "ITZ volume fraction in concrete with spheroidal aggregate particles and application: Part I. Numerical algorithm." *Magazine of Concrete Research*, 63, 473–482.

Zhu, Z., Provis, J., and Chen, H. (2018). "Quantification of the influences of aggregate shape and sampling method on the overestimation of itz thickness in cementitious materials." *Powder technology*, 326, 168–180.

List of Tables

TABLE 1. Chemical composition of used materials [wt.%]

Material	**CaO**	**SiO_2**	**Al_2O_3**	**Fe_2O_3**	**MgO**	**Na_2O**	**K_2O**	**SO_3**	**Loss on ignition (LOI)**
CEM I 52.5 R	63.2	20.61	5.33	2.36	1.49	0.21	0.41	3.39	1.63
Quartz sand	0.1	96	1.4	0.4	-	-	-	-	0.19
Limestone sand	55.02	0.11	0.27	0.22	-	-	-	-	43.7

TABLE 2. Physical properties of cement and aggregates

Material	**Specific density [g/cm^3]**	**Surface area [m^2/kg]**	**Water absorption [wt.-%]**
CEM I 52.5 R	3.14	5780	-
Quartz sand	2.67	760	0.5
Limestone sand	2.76	880	0.7

(Note: water absorption was measured according to EN 1097-6.)

TABLE 3. Mix composition for ITZ investigation

Specimen	Cement (g)	Quartz sand (g)	Limestone (g)	Water (g)	SP* (g)	w/c ratio
Quartz04	10	5	-	4	0.1	0.4
Quartz06	10	5	-	6	-	0.6
Limestone04	10	-	5	4	0.1	0.4
Limestone06	10	-	5	6	-	0.6

* Superplasticizer

List of Figures

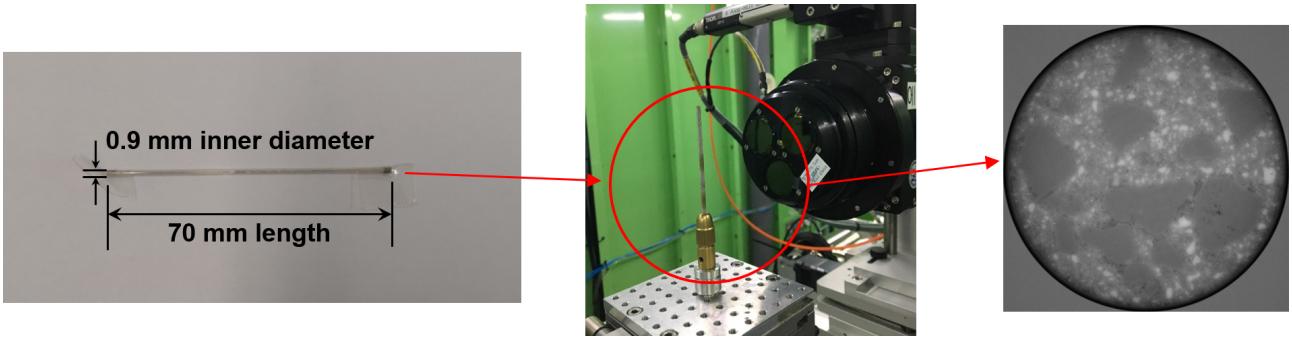

Fig. 1. Thin specimen for ITZ measurement (left), specimen setup in the micro CT image facility at PAL (Korea) (middle), and a cross-sectional micro-CT image (right).

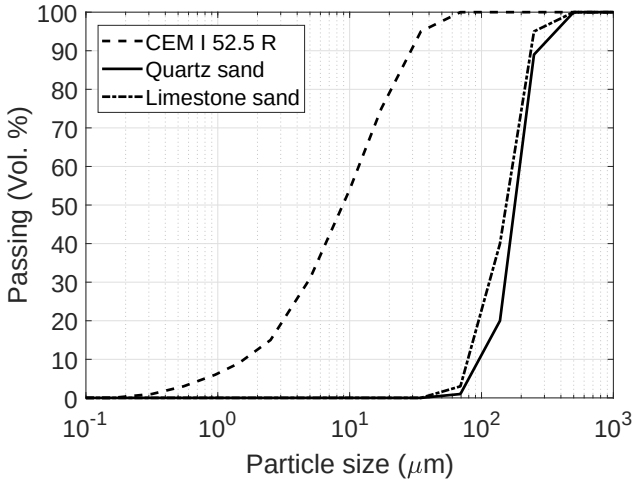

Fig. 2. Particle size distributions of cement and quartz and limestone sands (Note: for the measurements, laser granulometer and sieving were used for cement and sands, respectively.)

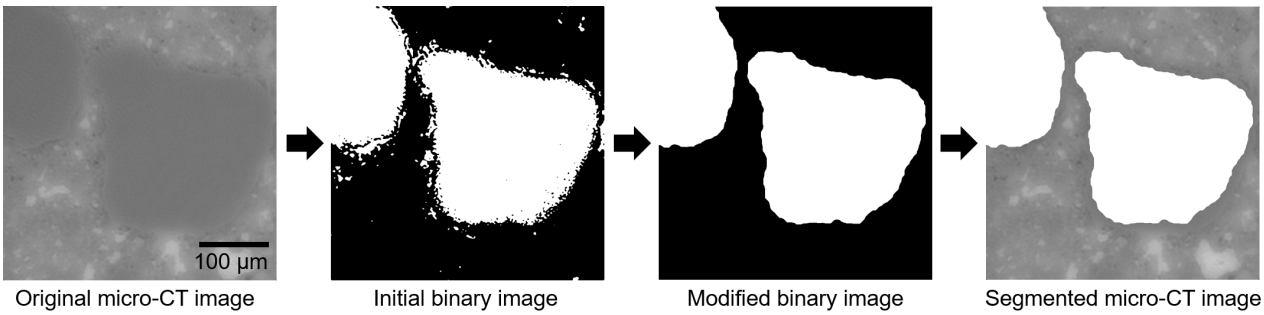

Fig. 3. Micro-CT imaging used to classify aggregate particles from the original image: (a) original micro-CT image; (b) initially binarized image; (c) modified binary image; (d) segmented micro-CT image. The white regions in (b)–(d) represent the aggregate particles.

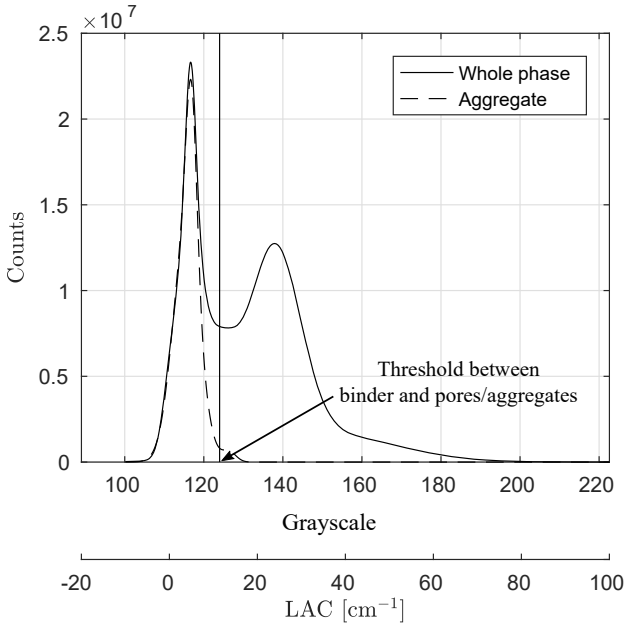

Fig. 4. Example for the thresholding process of binder and other components (aggregates and pores of the ROI of Quartz04)

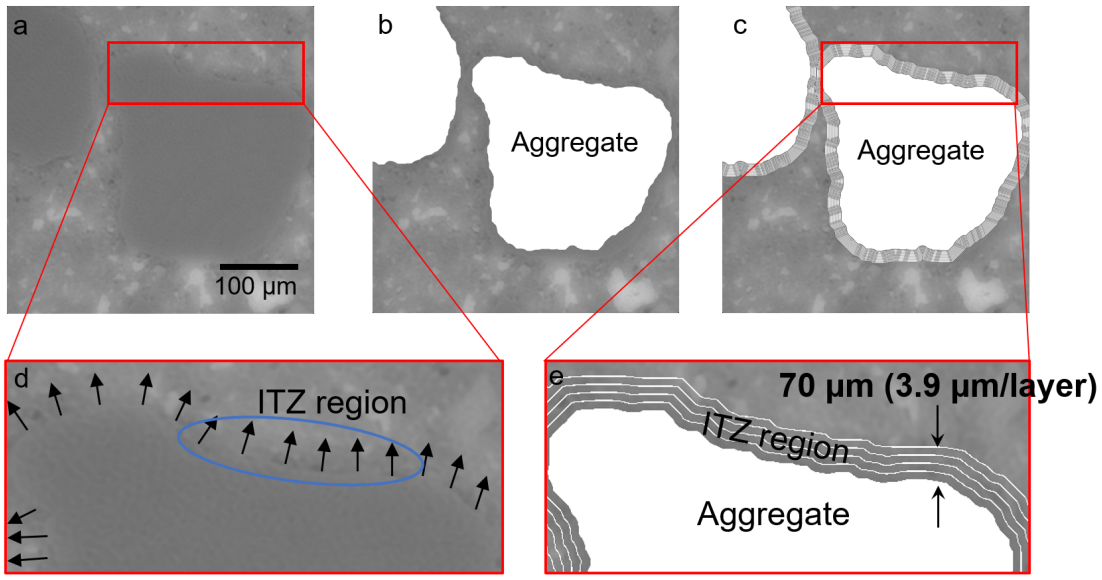

Fig. 5. Investigation of the ITZ using micro-CT imaging: (a) original micro-CT image; (b) segmented image; (c) ITZ investigation by layer; (d) magnification of the original image; (e) magnification of ITZ investigation by layer

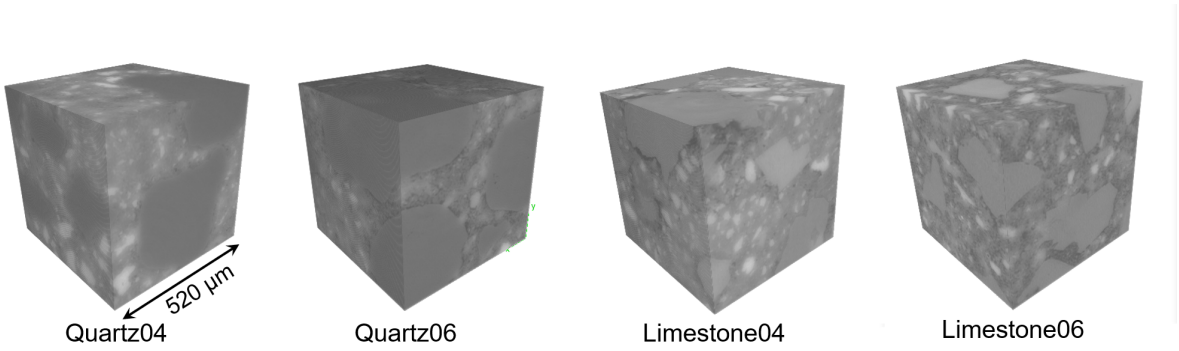

Fig. 6. ROIs of specimens with different conditions (Note: the side length of each specimen is 520 μm and is composed of 800 voxels with 0.65 μm resolution.)

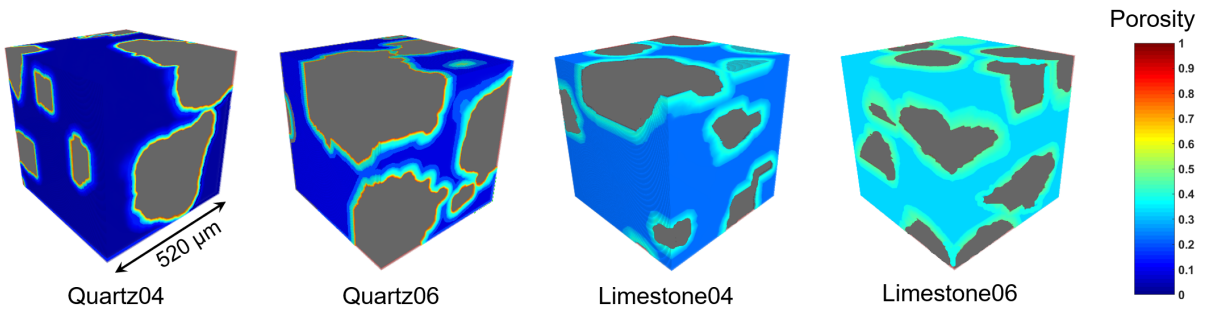

Fig. 7. Porosity distributions of specimens with different conditions (Note: in each image, the gray region represents aggregate particles.)

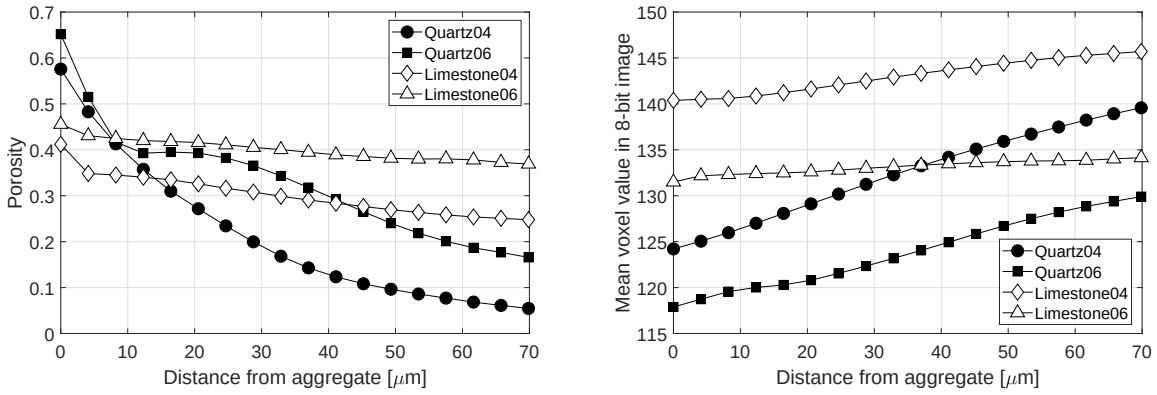

(a) (b)

Fig. 8. Characteristics of the ITZ with distance from aggregate in each specimen: (a) porosity; (b) mean voxel value.

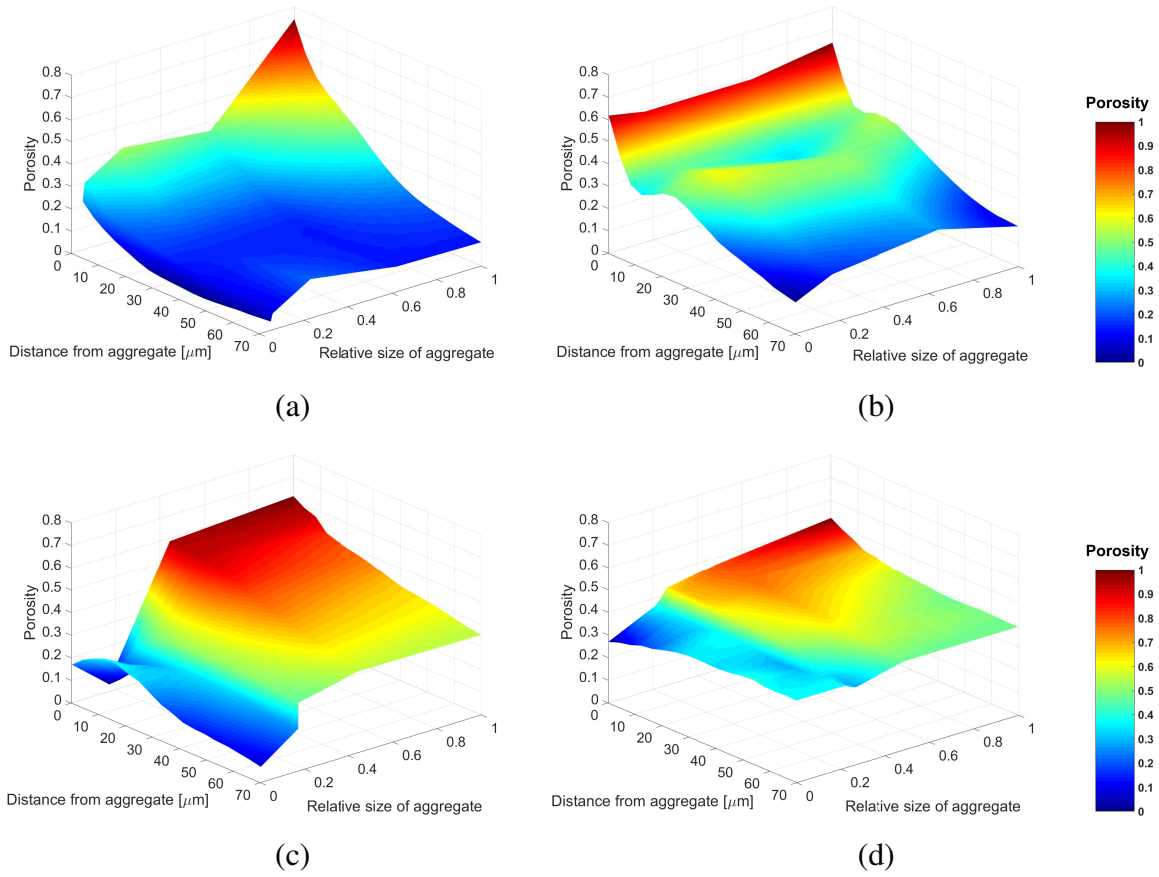

Fig. 9. Porosity distribution depending on aggregate size in each specimen: (a) Quartz04; (b) Quartz06; (c) Limestone04; (d) Limestone06.

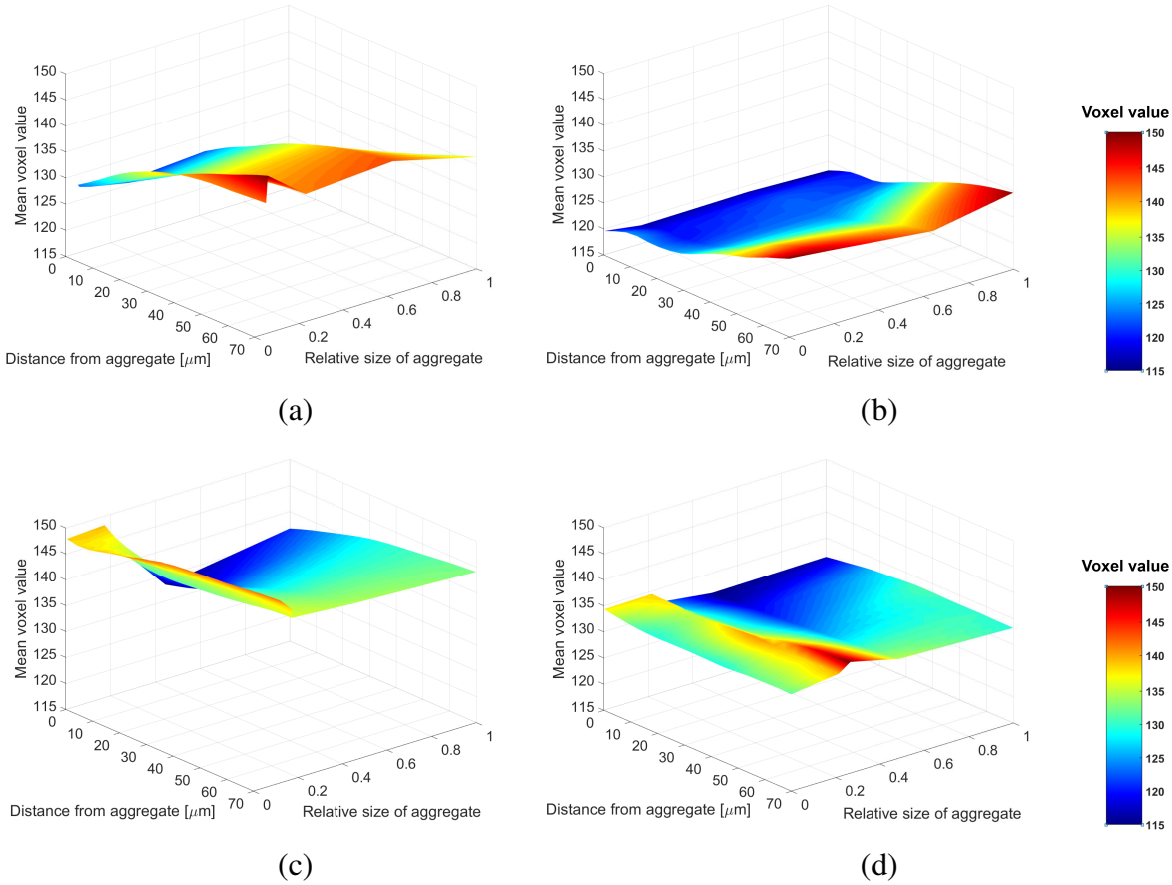

Fig. 10. Distribution of mean voxel value depending on aggregate size in each specimen: (a) Quartz04; (b) Quartz06; (c) Limestone04; (d) Limestone06.

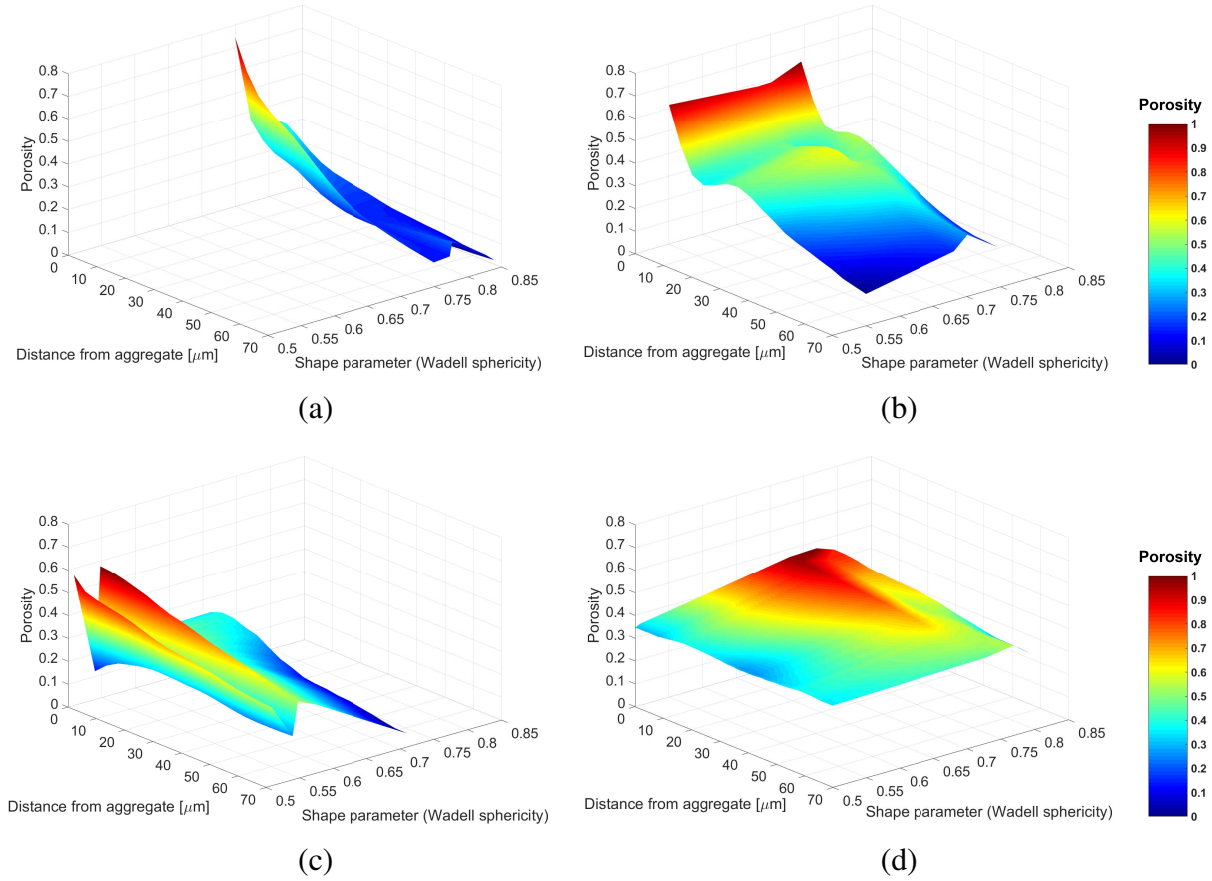

Fig. 11. Porosity distribution depending on sphericity values of aggregates: (a) Quartz04; (b) Quartz06; (c) Limestone04; (d) Limestone06.